Unsteady granular flows down an inclined plane

Stanislav Parez,[1,*] Einat Aharonov,[1] and Renaud Toussaint[2]
[1]*Institute of Earth Sciences, Hebrew University, Givat Ram, 91904 Jerusalem, Israel*
[2]*Institut de Physique du Globe de Strasbourg, École et Observatoire des Sciences de la Terre, Universite de Strasbourg, CNRS, 5 Rue Descartes, 67084 Strasbourg Cedex, France*
(Received 13 September 2015; revised manuscript received 19 January 2016; published 12 April 2016)

The continuum description of granular flows is still a challenge despite their importance in many geophysical and industrial applications. We extend previous works, which have explored steady flow properties, by focusing on unsteady flows accelerating or decelerating down an inclined plane in the simple shear configuration. We solve the flow kinematics analytically, including predictions of evolving velocity and stress profiles and the duration of the transient stage. The solution shows why and how granular materials reach steady flow on slopes steeper than the angle of repose and how they decelerate on shallower slopes. The model might facilitate development of natural hazard assessment and may be modified in the future to explore unsteady granular flows in different configurations.

DOI: 10.1103/PhysRevE.93.042902

I. INTRODUCTION

Accelerating and decelerating granular materials control many geophysical situations, with notable examples being landslides and geological faults. Understanding their flow would allow us to predict their energy and total deformation and estimate the risk of natural hazards. While steady granular flows are complex but relatively well understood, unsteady flows, prevailing in nature, still lack a theoretical description. Many fundamental questions regarding unsteady flows are still open. Under what conditions does a granular flow reach a steady state and why? How does the velocity profile evolve? What controls the time scale on which the flow accelerates and decelerates? What shear rate and shear stress control the energy dissipation? In this paper, we answer these questions for free-surface dry granular flows down a slope.

Our knowledge about granular flows mostly comes from laboratory experiments and computer simulations. As a result, three flow regimes have been classified [1–3]: solid, in which grains interact via long-lasting frictional contacts and deform slowly; gaseous, in which grains interact through collisions lasting briefly compared to the deformation time scale; and liquid, which is a transition between the two previous regimes. For a flow down a slope, the three regimes can be attained by changing the slope angle θ [4–6]. If θ is small, no flow is observed but only an elastic deformation, or the flow decelerates if it was already set in motion previously. Once θ exceeds the angle of repose, the flow accelerates. The increasing rate of collisions eventually leads to a steady flow. If, however, the slope is steep enough, the flow keeps accelerating because the energy that grains receive during a free fall between collisions exceeds the dissipation. Here we study the liquid regime, in which flow is possible yet not too vigorous.

Steady granular flows have been investigated for more than half a century, resulting in good knowledge of their rheology [2,7–10], flow regimes [3–5,11], scaling [12,13], and effects of boundary conditions [14–16]. On the other hand, unsteady flows have been discussed much less and have been described only approximately using depth-averaged models, also known as shallow water models. Depth-averaged models for granular flows arise from the depth-averaged mass and momentum conservation equations, originally derived by Savage and Hutter [19]. The resulting equations for mean velocity neglect spatial variation of velocity inside the moving body. Hence, the depth-averaged models are less accurate if the shear rate is large. Flow down a slope or channel flow was studied by [19–25], including analytical solutions for the evolution of mean velocity, front position, and thickness. These agree with experimental measurements [19,21,22,25] as long as the spatial fluctuations of velocity are small, but don't provide the profiles of stress and velocity.

Such profiles of velocity and stress are required to access energy dissipation and the associated destructive potential of the flow. In addition, the friction coefficient is known from physics and geophysics to depend on shear rate or relative sliding velocity between two surfaces [8–10,15,17,18]. Knowledge of shear rate could thus facilitate development of theoretical friction models.

Computer simulations allow examination of velocity profile and flow evolution, which are difficult to study experimentally. Acceleration down an inclined plane, sometimes followed by deceleration on a flat plane (landslide geometry), was addressed in [1,26–33] using the discrete element method (DEM). Results reveal that the (top) free surface moves faster than the bottom surface, shearing the mass completely throughout its thickness. Although the simulations show a long phase of acceleration and unsteady flow [33], the analytical solutions for velocity and stress profiles are known only for the steady flow [4,5,7,9,12,13]. Also, the duration of the accelerating flow before the steady flow is reached has not been investigated.

The present analytical solution describes granular flows under simple shear induced by gravity (see Fig. 1). The flow is uniform in both the lateral and longitudinal directions and the thickness h is kept constant. As a result, flow properties are functions of depth y and time t only. Simple shear geometry is simple enough to allow for an analytical solution yet describes essential features of many natural flows such as landslides, avalanches, or geophysical faults. These can often be approximated as two-dimensional chute flows, or as flow confined between two walls, with the parallel component of velocity dominating the other components. Note, however, that

*parezs@vscht.cz

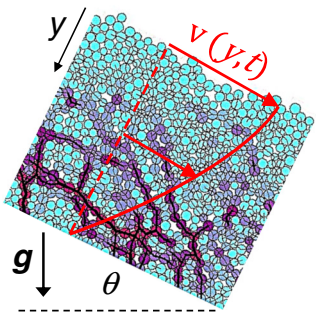

FIG. 1. Geometry of the studied system depicted on a snapshot from a DEM simulation. An infinitely-long granular layer accelerates down a slope inclined at an angle θ. The red envelope for the velocity vectors $v(y,t)$ denotes the velocity profile predicted by Eq. (11). The shades of the grains indicate contact stress: The dark grains are most stressed.

elongation and flattening of the flow (observed for landslides) is neglected here.

We first review equations describing the rheology of dry granular flows and derive the velocity field for the flow on an inclined plane (Sec. II). Then we introduce discrete element numerical simulations that serve as a test of our analytical model (Sec. III). Finally, we show that the analytical model reproduces the kinematics observed in simulations and we explain why, how, and at what time scale a flow reaches its final stage, be it steady state for accelerating flows or rest for decelerating flows (Sec. IV).

II. THEORY

Here we derive analytical forms of velocity, shear rate, and stress profiles for a granular flow of constant thickness down an inclined plane. Acceleration of the flow is a result of the action of gravitational and friction forces

$$\Phi_s \rho \frac{\partial v}{\partial t} = \Phi_s \rho g \sin\theta - \frac{\partial \tau}{\partial y}, \tag{1}$$

where θ is the inclination angle, $v(y,t)$ is the velocity along the flow direction, $\tau(y,t)$ is the shear stress, g is the gravitational acceleration, ρ is the grain mass density, and Φ_s is the solid fraction. We assume here that Φ_s is uniform with depth [4] and constant (a very weak dependence on flow velocity has been found [1,8,9,15]). As a result, the normal stress $N(y,t)$ is lithostatic: $N = \Phi_s \rho g \cos\theta y$.

To form a closed set of equations we need another relation between τ and v, i.e., a rheological law. We use the observation that friction in granular materials is shear rate dependent [8–10,17]. The only local dimensionless quantity for dry granular flows that contains shear rate is the so-called inertial number $I(y,t)$,

$$I = \frac{\dot\gamma d}{\sqrt{N/\rho}}, \tag{2}$$

where d is the grain size and $\dot\gamma(y,t)$ is the shear rate [the negative sign is because the y axis is pointing downward (see Fig. 1)]

$$\dot\gamma = -\frac{\partial v}{\partial y}. \tag{3}$$

The friction coefficient $\mu(y,t)$ (also dimensionless) can then be expressed as an expansion in I. The linearized version of the friction law is

$$\mu \equiv \frac{\tau}{N} = \tan\theta_r + \beta I, \tag{4}$$

where θ_r is the dynamic angle of repose and β is another material parameter ($\tan\theta_r \approx 0.35$ and $\beta \approx 0.6$ for glass beads [1]). This type of rheology, in which μ is a function of I, has been verified for a variety of systems and boundary conditions [1,8,9,22] and holds as long as plastic processes are negligible. Since β has been found positive, friction increases with shear rate under constant normal stress. The linear approximation (4) is valid for the liquid flow regime studied here, which corresponds to an inertial number of the order of 10^{-3}–10^{-1} [1,9]. For larger inertial numbers, the flow is collision dominated and eventually becomes turbulent. In this regime, the linear law breaks down.

The resulting shear stress $\tau = \mu N$ is

$$\tau = \tan\theta_r \Phi_s \rho g \cos\theta y + \rho \beta d \sqrt{\Phi_s g \cos\theta y}\,\dot\gamma. \tag{5}$$

The first term is rate independent and is usually of larger magnitude. The second term accounts for the increase of shear stress with shear rate. Consequently, friction force increases as the flow accelerates.

Taking the spatial derivative of Eq. (1) and using the constitutive relation (5), we arrive at a single equation for $\dot\gamma$,

$$\frac{\partial \dot\gamma}{\partial t} = \beta d \sqrt{\frac{1}{\Phi_s} g \cos\theta}\, \frac{\partial^2}{\partial y^2}(\sqrt{y}\dot\gamma). \tag{6}$$

This is a nonlinear diffusion equation for $\dot\gamma$. Note that a diffusion equation for shear rate was introduced in Ref. [15] and used to determine the transient time to obtain steady Couette flow in a simple shear cell. However, due to the addition of gravity here, the diffusion coefficient is nonuniform and thus the diffusion equation (6) is quite different from that in Ref. [15].

We will solve Eq. (6) along with the following boundary or initial conditions:

$$\tau(0,t) = 0, \tag{7a}$$

$$v(h,t) = 0, \tag{7b}$$

$$v(y,0) = v^0(y), \tag{7c}$$

where h is flow thickness. The boundary conditions can be stated as the top surface of the flow is free of stresses [Eq. 7(a)], the velocity at the bottom of the flowing mass is zero (the ground surface is rough) [Eq. 7(b)], and the initial velocity is $v^0(y)$ [Eq. 7(c)].

The solution is found as a series solution using separation of variables and superposition of all linearly independent solutions [34] (let us suppose for now that the spectrum of

solutions is discrete: $n = 0,1,\ldots$)

$$\dot{\gamma} = \sum_n p_n(t) q_n(y), \tag{8}$$

where

$$\frac{dp_n}{dt} = K_n p_n, \quad \frac{d^2(\sqrt{y}q_n)}{dy^2} = \frac{K_n}{\beta d\sqrt{\frac{1}{\Phi_s} g\cos\theta}} q_n.$$

The separation constants K_n are to be determined from the boundary conditions.

The functions p_n are exponentially growing for $K_n > 0$. Because we are looking for a solution that is stable, the K_n are restricted to be nonpositive: $K_0 = 0$ and $K_n \equiv -1/T_n < 0$ for $n > 0$, where T_n are positive constants with a dimension of time. The spatial functions q_n have two independent solutions: the Bessel functions of the first and the second kind, $J_{2/3}$ and $Y_{2/3}$ [35]. For small y, they behave as $\sim\sqrt{y}$ or $\sim 1/\sqrt{y}$. To satisfy the boundary condition 7(a), we have to exclude the divergent solution. This leads to the following expansion for shear rate:

$$\dot{\gamma} = \begin{cases} b^*\sqrt{y} + \sqrt{h}\sum_n b_n J_{2/3}\left(\kappa_n\left(\frac{y}{h}\right)^{3/4}\right)e^{-t/T_n}, & \theta > \theta_r \quad (9a) \\ \sqrt{h}\sum_n b_n J_{2/3}\left(\kappa_n\left(\frac{y}{h}\right)^{3/4}\right)e^{-t/T_n}, & \theta < \theta_r, \quad (9b) \end{cases}$$

where b^* and b_n are yet undetermined weights, $J_{2/3}(z)$ is a Bessel function of the first kind [35], and κ_n is a dimensionless constant related to T_n by

$$\kappa_n = \frac{4}{3}\left(\frac{\Phi_s h^3}{T_n^2\beta^2 d^2 g\cos\theta}\right)^{1/4}. \tag{10}$$

Each term in Eq. (9) is a solution of Eq. (6) that satisfies the boundary condition 7(a). If the inclination angle is larger than the angle of repose $\theta > \theta_r$, the flow accelerates towards a steady state. In that case, we allow for the time-independent solution $b^*\sqrt{y}$ (the first term), which corresponds to the steady flow shear rate since all other terms vanish after sufficient time. Note that this term is identical to the Bagnold shear rate profile, found in numerous studies of steady granular flows on an incline [4,5,7]. For $\theta < \theta_r$ the flow decelerates towards rest as $\dot{\gamma}(t\to\infty)\to 0$. Therefore, the time-independent term is discarded.

The spatial integration of $-\dot{\gamma} = \frac{\partial v}{\partial y}$ yields velocity up to an integration constant, which is allowed to be a function of time. The integration constant is determined from Eq. (1) using the series 9(a) or 9(b) in Eq. (5). This leads to the velocity formula

$$v(y,t) = \begin{cases} \frac{2}{3}b^*(h^{3/2} - y^{3/2}) + \frac{16}{9}h^2\sum_n \frac{b_n}{\kappa_n^2}\frac{d}{dy}\left[\sqrt{y}J_{2/3}\left(\kappa_n\left(\frac{y}{h}\right)^{3/4}\right)\right]e^{-t/T_n}, & \theta > \theta_r \quad (11a) \\ -g\cos\theta(\tan\theta_r - \tan\theta)t + \frac{16}{9}h^2\sum_n \frac{b_n}{\kappa_n^2}\frac{d}{dy}\left[\sqrt{y}J_{2/3}\left(\kappa_n\left(\frac{y}{h}\right)^{3/4}\right)\right]e^{-t/T_n}, & \theta < \theta_r, \quad (11b) \end{cases}$$

where b^* is

$$b^* = \frac{\sqrt{\Phi_s g\cos\theta}(\tan\theta - \tan\theta_r)}{\beta d}. \tag{12}$$

The solution 11(b) is valid as long as $v(y,t) > 0$. Once the velocity at given depth y decays to zero, the layer becomes locked due to static friction and $v(y) = 0$ afterward.

To satisfy the boundary condition 7(b), $v(h,t) = 0$, for arbitrary weights b_n, all terms in Eq. (11) must vanish for $y = h$. This constrains the values of κ_n, and consequently T_n, so as to satisfy

$$\frac{d}{dy}\left[\sqrt{y}J_{2/3}\left(\kappa_n\left(\frac{y}{h}\right)^{3/4}\right)\right]\Big|_{y=h} = 0, \quad T_n = \frac{16\sqrt{\Phi_s}}{9\kappa_n^2}\frac{h^{3/2}}{\beta d\sqrt{g\cos\theta}}, \quad n = 1,2,\ldots,\infty. \tag{13}$$

In other words, κ_n are points where the function $\sqrt{z}J_{2/3}(z)$ has an extreme value. Since this function oscillates, we have an infinite and discrete number of solutions and therefore n is indeed identified with natural numbers. The first few values of κ_n and T_n/T_1 are given in Table I.

Finally, the constants b_n are determined from the initial condition (7c) as

$$b_n = \begin{cases} -\frac{\int_0^h(\sqrt{y}dv^0/dy + b^*y)J_{2/3}(\kappa_n(y/h)^{3/4})dy}{\sqrt{h}\int_0^h J_{2/3}^2(\kappa_n(y/h)^{3/4})\sqrt{y}dy}, & \theta > \theta_r \quad (14a) \\ -\frac{\int_0^h \sqrt{y}dv^0/dy J_{2/3}(\kappa_n(y/h)^{3/4})dy}{\sqrt{h}\int_0^h J_{2/3}^2(\kappa_n(y/h)^{3/4})\sqrt{y}dy}, & \theta < \theta_r. \quad (14b) \end{cases}$$

In the preceding relation we used Eq. (9) and orthogonality of q_n for different n (see the Appendix): $\int_0^1 \sqrt{z}J_{2/3}(\kappa_n z^{3/4})J_{2/3}(\kappa_m z^{3/4})dz \sim \delta_{nm}$. In Table I we give a few values of b_n corresponding to the initial velocity $v^0 = 0$ (flow accelerating from rest) or $v^0 = 2b^*(h^{3/2} - y^{3/2})/3$ (flow decelerating from a steady state). While the absolute values of T_n

and b_n depend on the system dimensions, material properties, and inclination angle, their relative values are universal. Note the rapid decay of T_n and b_n with increasing n.

In general, one needs to calculate b_n for all n for which the factor $\exp(-t/T_n)$ is greater than a desired accuracy. Using these b_n in Eqs. (11) and (9) gives accurate profiles of the velocity and shear rate fields [and also the shear stress field related by Eq. (5)]. Nevertheless, for a first-order approximation, when we restrict the calculation to the $n = 1$ term only, the velocity field Eq. (11) simplifies to

$$v(y,t) = \begin{cases} \frac{2}{3}b^*(h^{3/2} - y^{3/2})(1 - e^{-t/T_1}), & \theta > \theta_r \quad (15a) \\ -g\cos\theta(\tan\theta_r - \tan\theta)t + v^0(y)e^{-t/T_1}, & \theta < \theta_r. \quad (15b) \end{cases}$$

T_1 is calculated from Eq. (13) using κ_1 from Table I, while b^* is calculated from Eq. (12). The corresponding shear rate and shear stress fields can be derived using their definitions (3) and (5).

III. SIMULATIONS

Numerical simulations were used as a benchmark for the theory derived above. They employ the DEM [36], in which the Newtonian equations of motion for a set of grains are solved in discrete steps. Grains are modeled as balls with rotational and translational degrees of freedom. They interact via viscoelastic contact forces according to the Hertz-Mindlin contact model [37,38]

$$F_{ij}^n = \frac{\sqrt{2}E}{3(1-\nu^2)}\sqrt{R_{ij}\xi_{ij}}\xi_{ij} - \gamma\sqrt{R_{ij}\xi_{ij}}\dot{\xi}_{ij},$$
$$F_{ij}^t = \min\left[\frac{2\sqrt{2}E}{(2-\nu)(1+\nu)}\sqrt{R_{ij}\xi_{ij}}\Delta s, \mu_{gg}F_{ij}^n\right], \quad (16)$$

where F_{ij}^n and F_{ij}^t are normal and shear components of the contact force between interacting grains i and j, R_{ij} is the harmonic mean of the grains' radii, and ξ_{ij} is the overlap between the two grains. An elastic modulus $E = 1.31\times10^{10}$ Pa and Poisson ratio $\nu = 0.235$ were chosen to simulate quartz grains with density $\rho = 2.5\times10^3$ kg m^{-3}. Energy dissipation is governed by the normal damping force (the second term in F_{ij}^n) with damping coefficient $\gamma = 0.8$ and by the tangential friction F_{ij}^t. The restitution coefficient is not constant, but depends on velocities of colliding grains [37]. The tangential force is initially elastic, calculated from shear displacement Δs on contacts of the grains from the instant the contact was formed. Once the spring force exceeds the Coulomb friction criterion, the contact starts sliding with a constant shear force $F_{ij}^t = \mu_{gg}F_{ij}^n$, where the grain-grain friction coefficient is $\mu_{gg} = 0.5$. Note that the grain-grain friction coefficient is not the same as the macroscopic dynamic friction coefficient [39,40], which is investigated below and found to be shear rate dependent.

Grain diameters were randomly drawn from a Gaussian distribution with both mean value and standard deviation equal to d. The distribution was however cut, so all diameters fall within $0.8d$–$1.2d$. Equations of motion were integrated using the velocity Verlet algorithm [41] with a time step $0.1d\sqrt{\rho/E}$ small enough to resolve grain-grain collisions.

Periodic boundary conditions were applied in the direction of the flow, which is equivalent to the constant thickness boundary condition used in the theory. The width of the simulation box along the flow direction was $96d$ (no size effects due to this scale were observed), while the thickness of the flow varied among different simulations between $h = 12d$ and $96d$ to test the volumetric scaling.

Granular systems are initiated as layers with random loose packing, standing on a rough horizontal surface made of glued grains. Subject to vertical gravitational acceleration, the grains sediment. By gradually turning the slope on which material flows, the static angle of repose $\theta_{sr} = 17^\circ$ and the dynamic angle of repose $\theta_r = 14^\circ$ were found. To study acceleration we used inclination angles $\theta = 17^\circ$–25°. The selected range of angles can accommodate steady flows (see Refs. [4,5,11] for a phase diagram of flow regimes). Larger inclination angles lead to unstable acceleration and breakdown of the liquid flow regime. To study deceleration we turn the slope down to an angle $\theta < \theta_r = 14^\circ$.

TABLE I. Parameters κ_n, T_n, and b_n used in the expansions in Eqs. (9) and (11). The b_n^a and b_n^d given here correspond to the initial velocity $v^0 = 0$ (for a flow accelerating from rest) and $v^0 = 2b^*(h^{3/2} - y^{3/2})/3$ (for a flow decelerating from a steady state), respectively. While the absolute values of T_n and b_n depend on the system dimensions, material properties, and inclination angle, their relative values given below are universal.

n	κ_n	T_n/T_1	b_n^a/b^*	b_n^d/b^*
1	1.87	1	−1.30	1.30
2	4.99	0.14	0.30	−0.30
3	8.12	0.053	−0.14	0.14

IV. RESULTS

A. Flow density

The derivation of the flow velocity carried out in Sec. II relies on the presumption that the solid fraction Φ_s is constant and uniform throughout the granular layer. In fact, Φ_s is a weak function of I [1,8,9,15], however, its variation can be neglected compared to variations of velocity and shear stress. This point is illustrated in Fig. 2, where we show solid fraction profiles at a number of time instants during a simulation of $h = 96d = 9.6$-m-thick flow. The flow first accelerates on a 17° slope starting from rest. After reaching the steady state, the slope is turned down to 0° and the flow decelerates on a flat plane. The solid fraction at all instants of the simulation remains the same within its fluctuations, while, as we will see later, velocity and shear stress vary significantly.

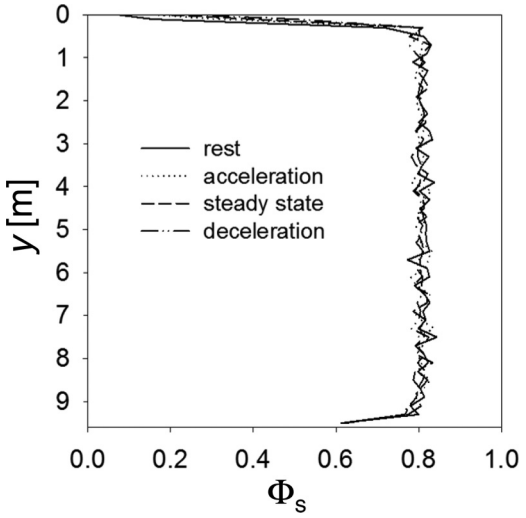

FIG. 2. Solid fraction profiles recorded in a simulation of an $h = 96d = 9.6$-m-thick flow accelerating on a $\theta = 17^\circ$ slope and decelerating on a flat plane thereafter. The profiles were taken at times when the system starts flowing (—), in the middle of the acceleration stage ($\cdots$), on reaching the steady flow ($- - -$), and in the middle of the deceleration stage ($- \cdot\cdot -$). The shown two-dimensional solid fraction of 0.80 can be mapped to a three-dimensional solid fraction of 0.54 [27].

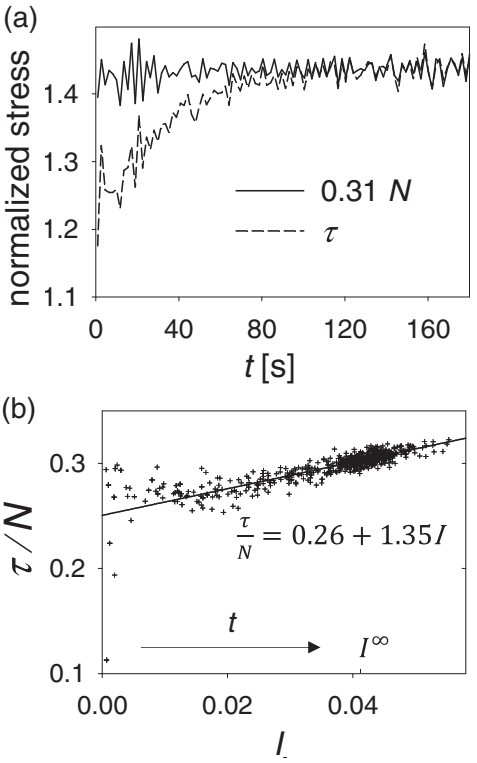

FIG. 3. (a) Depth averaged shear and normal stress evolution observed in a DEM simulation of the flow with $h = 96d = 9.6$ m and $\theta = 17^\circ$. The normal stress is multiplied by the steady-state friction coefficient $\tan 17^\circ = 0.31$ to match the steady-state shear stress value. (b) Friction coefficient τ/N as a function of inertial number I for the same system. Points are simulation data at a series of time instants during the acceleration. The course of time is indicated by the arrow. The solid line is a fit to Eq. (4), resulting in $\tan\theta_r = 0.26 \pm 0.01$ and $\beta = 1.35 \pm 0.08$, where the uncertainty of the fit was calculated based on the deviation among values for different y.

B. Stress evolution and flow stability

Here we verify and calibrate the rheological law (4). Figure 3(a) shows depth-averaged shear and normal stresses as functions of time. The data were obtained from a DEM simulation for $\theta = 17^\circ > \theta_r$, i.e., the flow accelerates towards a steady state. While the normal stress is constant and equal to lithostatic stress $N = \Phi_s \rho g \cos\theta y$, the shear stress increases from its minimum value $\lim_{\dot\gamma\to 0}\tau = \tan\theta_r \Phi_s \rho g \cos\theta y$ [see Eq. (5)] towards the steady flow value $\tau = \Phi_s \rho g \sin\theta y$, which can be derived from Eq. (1). Similarly, the friction coefficient $\mu = \tau/N$ (not shown) evolves following the evolution of τ.

Figure 3(b) shows the $\mu(I)$ rheology, i.e., the friction coefficient μ increases linearly with the inertial number I, in accordance with Eq. (4). The linear dependence between μ and I is found for the whole range of angles leading to a stable flow and for all studied system dimensions, $d = 0.001$–0.1 m and $h = 12d$–$96d$, indicating a liquidlike regime of the flow.

The rheological parameters θ_r and β are independent of depth except for close to the ground surface $y = h$, so Eq. (4) holds locally. On the other hand, the parameters are found to moderately depend on the thickness for thin layers (with thickness a few times d) due to nonlocal effects [42]. In addition, β varies with θ. In simulations, increasing θ from 17° to 25° results in the decrease of β by 40%.

Based on Fig. 3, we can understand why a flow can reach a steady state. According to Eq. (1), acceleration of the flow is given by the difference between the driving gravitational force $g\sin\theta$ and the resisting friction force $\partial\tau/\partial y$. This difference is non-negative only if $\theta > \theta_r$ (if the flow starts from rest, a larger static friction angle θ_{sr} needs to be overcome). As the flow accelerates, $\dot\gamma$ increases due to increasing v. In line with Eq. (5), increasing $\dot\gamma$ leads to increasing τ and therefore increasing $\partial\tau/\partial y$. Eventually, the friction force $\partial\tau/\partial y$ balances the gravitational force. At that moment the acceleration vanishes and the flow reaches a steady state. From then on, friction and inertial number fluctuate around their constant steady flow values ($I^\infty = 0.041$ and $\mu^\infty = 0.31 = \tan 17^\circ$ for the system shown in Fig. 3).

Note that for the Coulomb friction law, i.e., $\beta = 0$, shear stress is independent of velocity [see Eq. (5)] and thus constant with time. Such a system would accelerate unstably with uniform and constant acceleration $g\cos\theta(\tan\theta - \tan\theta_r) > 0$ and would not reach steady flow apart from the special case $\theta = \theta_r$.

C. Flow velocity

Figures 4 and 5 show velocity for a flow accelerating from rest (top) and decelerating from a steady state (bottom). The theoretical prediction (11) (dashed lines), in which we neglect all terms with $n > 3$, is tested against the DEM simulation results (solid lines).

Figure 4 shows velocity profiles at discrete time instants. The flow is nonuniform, shearing the mass throughout its thickness. If $\theta > \theta_r$ the flow accelerates, eventually reaching

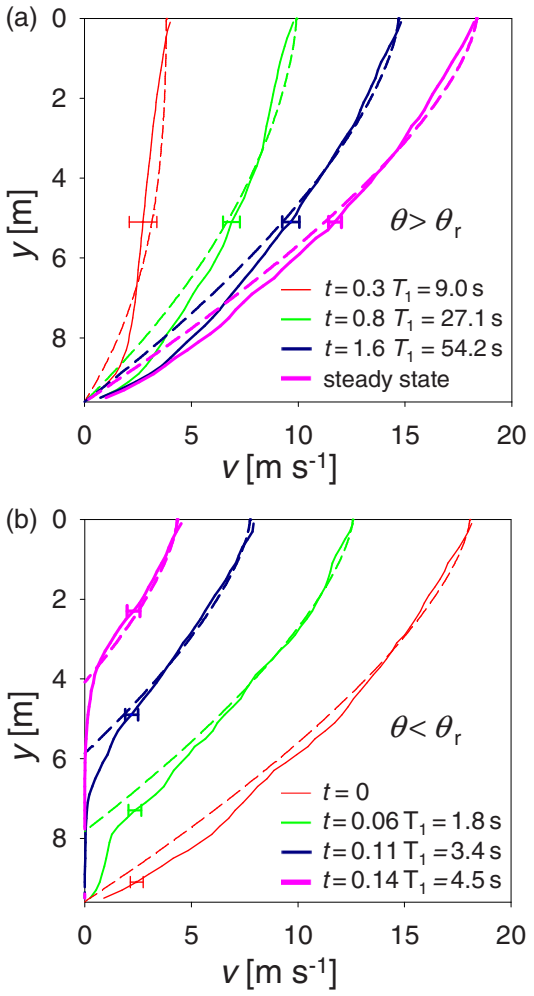

FIG. 4. Velocity profiles at various time instants during (a) acceleration down a slope of $\theta = 17^\circ$ and (b) deceleration on a flat plane $\theta = 0^\circ$. The times at which profiles were recorded increase with the line thickness [from left to right in (a) and from right to left in (b)]. The solid lines are simulation results, while the dashed lines are analytical predictions of Eq. (11) for the granular flow with $h = 96d = 9.6$ m and the angle of repose $\theta_r = 14^\circ$. In the case of the accelerating flow (a), the time T_1 characterizes the time required to reach the steady flow. The error bars indicate uncertainties of velocity profiles associated with different initial configurations.

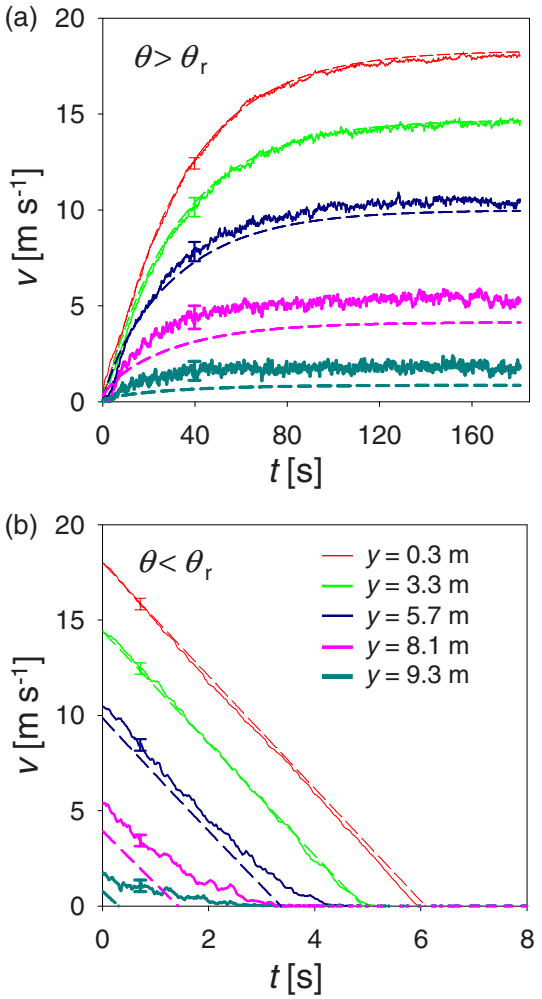

FIG. 5. Velocity evolution during (a) acceleration down a slope of $\theta = 17^\circ$ and (b) deceleration on a flat plane $\theta = 0^\circ$. Each line is velocity at a depth $y = 0.3$–9.3 m, where the depth increases from the upper line towards the lower line, inside the $h = 96d = 9.6$-m-thick flow. The solid lines are simulation results, while the dashed lines are analytical predictions of Eq. (11). Note that deceleration (b) is not the reversed evolution of acceleration (a). The error bars indicate uncertainties of velocity associated with different initial configurations.

the steady state. The steady flow profile (magenta line) is given by the first term in Eq. 11(a) and is consistent with the Bagnold rheology studied in previous works [4,5,7,12,13].

If $\theta < \theta_r$, the flow decelerates. For the given flow parameters ($h = 96d = 9.6$ m, $g = 9.8$ ms^{-2}, and $\theta = 17^\circ$), the deceleration rate is approximately uniform and constant, as the first term in Eq. 11(b) dominates the evolution. Once velocity at a given depth y decays to zero, the layer becomes locked due to static friction and $v(y) = 0$ thereafter. Since deeper layers have lower velocity, they stop first. Consequently, the flow becomes increasingly limited, confined to a gradually thinning layer near the top surface.

Figure 5 shows complementary plots of velocity evolution at a number of different depths. If $\theta > \theta_r$, the velocity approaches the steady flow velocity as a series of exponentially decaying functions with characteristic times T_n. By time T_1 (=33 s for the system in the figure) all terms in the series in Eq. (11) with $n > 1$ vanish (see Table I for relative values of T_n) and the $n = 1$ term dominates the time evolution. Acceleration decays as $\sim \exp(-t/T_1)$ and velocity increases approximately as $\sim 1 - \exp(-t/T_1)$.

If $\theta < \theta_r$, velocity decays towards zero. For the case $\theta = 0$ shown in Fig. 5(b), the deceleration is considerably faster compared to the acceleration down a slope of $\theta = 17^\circ$ shown in Fig. 5(a), due to the presence of $-g \tan\theta_r t$ in Eq. 11(b). The leading $n = 1$ term in the series in Eq. 11(b) satisfies $t \ll T_1$ and can be expanded linearly as $\sim 1 - t/T_1$. The remaining terms in the series can be neglected because of small $\exp(-t/T_n)$ and/or b_n. As a consequence, the velocity decreases approximately linearly with time.

The overall fit between the theory and the simulations is very good, lending confidence to the theory. However, there is a noticeable deviation between the simulation and the theoretical curves in Figs. 4 and 5, mostly near the bottom surface. This deviation does not result from a time fluctuation or statistical uncertainty, as shown by error bars presenting the variability from different initial configurations. In the acceleration phase [Figs. 4(a) and 5(a)] the deviation is due to a difference in boundary conditions. In simulations, the motion of the deepest flowing grains, subject to largest shear and normal stresses, is intermittent and alternates between stick and slip stages. This is not perfectly consistent with the no-slip boundary condition used in the theory for brevity of analytical calculations. For the deceleration phase [Figs. 4(b) and 5(b)] the simulation velocity profiles have exponentially decaying tails penetrating beyond the stop depth. This feature was explained by Kamrin and Koval [43] to be a nonlocal effect (not included in the present rheological law), in which the flow above the stop depth induces a limited flow in deeper layers despite shear stress being lower than the yield stress.

Perhaps counterintuitively, deceleration is not the reversed time evolution of acceleration. The difference between the $\theta > \theta_r$ and $\theta < \theta_r$ solutions originates from the existence of a time-independent term in the expansion (8). For $\theta > \theta_r$, the time-independent term is allowed and is identical to the steady shear rate profile $b^*\sqrt{y}$ reached after the remaining exponentially decaying terms vanish. For $\theta < \theta_r$, the time-independent term vanishes as there is not a strong enough driving force to maintain steady flow.

D. Transient time and its scaling

During acceleration, velocity approaches the steady flow profile as a series of exponentially decaying functions with characteristic times T_n [see Eq. (11)]. According to Eq. (13), the relative magnitudes $T_n/T_m = \kappa_m^2/\kappa_n^2$ are universal, independent of flow dimensions or inclination angle, since the κ_n are constants equal to points of extrema of the function $\sqrt{z}J_{2/3}(z)$. Because T_1 is sufficiently larger than the other T_n (see Table I), it dominates the time evolution after the very initial period. Therefore, T_1 is an appropriate scale of the duration of the acceleration stage.

In Fig. 6 (points) we plot the transient time T_1 obtained by fitting $\sim\exp(-t/T_1)$ to simulation data for $v(y,t) - v(y,t \to \infty)$. The simulations were run for various values of h, d, and θ. Results are compared to the analytical prediction (solid line) given by Eq. (13) and the expected scaling $T_1 \sim h^{3/2}/\beta d\sqrt{g\cos\theta}$ is recovered. Thus, T_1 increases with flow thickness as $\sim h^{3/2}$ and decreases with grain diameter as $\sim d^{-1}$, i.e., in the same way as the steady flow velocity. The scaling with θ is more complex than $\sim 1/\sqrt{\cos\theta}$ because β also varies with θ. The decrease of β by 40% was found on increasing θ from 17° to 25° in our simulations. In addition, T_1 is not expected to vary significantly with mechanical characteristics of grains, such as restitution coefficient, grain-grain friction coefficient, or elastic modulus, as these were shown to have a small influence on the flow rheology [9].

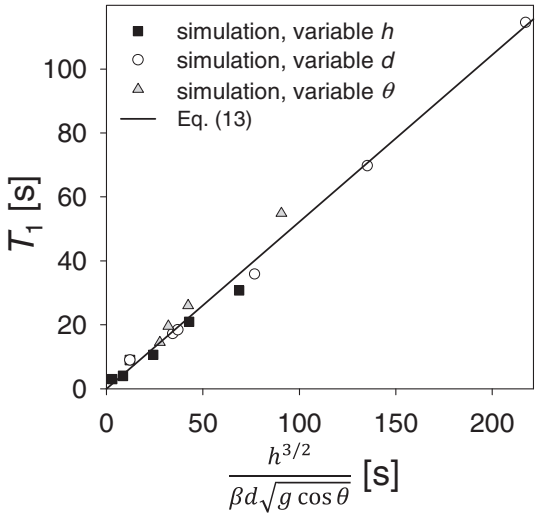

FIG. 6. Scaling of T_1, the characteristic acceleration time scale, with flow thickness h, average grain size d, and inclination angle θ. Points are simulation results for systems with $h = 12d$–$96d$, $d = 0.1$ m, and $\theta = 17°$ (squares); $h = 48d$, $70d$, or $96d$, $d = 0.1$–1 m, and $\theta = 17°$ (circles); and $h = 48d$, $d = 0.1$ or 1 m, and $\theta = 18°$–$25°$ (triangles). The solid line is the analytical prediction (13).

V. CONCLUSION

While significant progress has been made in the continuum description of steady granular flows over the past decade, unsteady flows have been much less discussed, despite their importance in geophysical and industrial processes. In this work we solved the kinematics of a granular flow of constant thickness on an inclined plane. We analytically derived velocity and stress fields for both accelerating flows, when the slope angle θ is larger than the angle of repose θ_r (but still is shallow enough to reach a steady state), and decelerating flows, in the opposite case. We compared the analytical derivation to two-dimensional DEM simulations of flow down inclines.

Similarly to steady flows, we found that friction resistance is an approximately linearly increasing function of shear rate. For $\theta > \theta_r$ the shear rate increases as the flow accelerates until the resisting friction force balances the originally prevailing gravitational force. At that moment the net force is zero and the flow reaches a steady state. The velocity was found to increase towards the steady flow velocity profile $v^\infty(y)$ (consistent with the Bagnold scaling) approximately as

$$v(y,t) \approx v^\infty(y)(1 - e^{-t/T_1})$$

for accelerating flow. The transient time T_1, which characterizes the duration of the acceleration, was found (both analytically and in DEM simulations) to be controlled by granular layer thickness h, grain size d, slope angle θ, gravitational acceleration g, solid fraction Φ_s, and rheological parameter β,

$$T_1 = 0.5\sqrt{\Phi_s}\,\frac{h^{3/2}}{\beta d\sqrt{g\cos\theta}}.$$

For $\theta < \theta_r$ the flow decelerates. Deceleration is not a reverse time image of acceleration, since it includes an extra deceleration rate $-g\cos\theta(\tan\theta_r - \tan\theta)$ that is not present

during acceleration. As a result, the deceleration stage is faster than that of acceleration for a given flow. During deceleration, a first-order approximation of the velocity, as it decays from the initial velocity v^0, was shown to be

$$v(y,t) \approx v^0(y)e^{-t/T_1} - g\cos\theta(\tan\theta_r - \tan\theta)t.$$

Discrete element method simulations showed that the first-order approximations of the transient velocity fields provide a good fit, except for the very initial stage when fast decaying corrections are important. To solve the velocity field (and the related shear rate and shear stress fields) more accurately, Eqs. (11)–(14) were used.

Several insights are gained from the present theoretical analysis regarding the transient time T_1 to reach steady state in gravity driven flows on an incline.

(i) The transient time increases with flow thickness as $\sim h^{3/2}$. This is a weaker dependence compared to $\sim h^2$ found for Couette flow in a simple shear cell [15].

(ii) The transient time depends inversely on β. This implies that the less shear strengthening the flow is (i.e., smaller β), the longer it takes the flow to reach a steady state. For slopes exceeding θ_r the flow will never reach a steady state if stress is independent of shear rate (i.e., if $\beta = 0$).

(iii) It is possible to assess the transient times in natural systems, e.g., landslides: Assuming $\theta = 35^\circ$, $d = 1$ cm, and $\Phi_s = 0.6$, the time scales are expected to be of the order of $T_1 = 0.7$, 23, and 720 s for flowing layers of thickness of $h = 0.1$, 1, and 10 m, respectively. For this calculation we used $\beta = 0.6$ from granular experiments with glass beads [1]. Clearly, the transient time is sensitive to the thickness of the flow. For the 10-m-thick flow the transient time is several minutes, which exceeds the duration of flows on natural slopes. It was thus predicted that thick landslides do not reach steady flow.

(iv) Acceleration and declaration are not symmetrical: Acceleration to steady flow takes longer than it takes to stop the same flow. In addition, the geometry of acceleration and deceleration is not symmetrical: While flow accelerates eventually through the depth of the layer, stopping occurs from the bottom upward, so that flow becomes confined to an increasingly thinning layer near the top, while the bottom grains have already stopped.

These results will hopefully prove useful for understanding and predicting natural and industrial flows.

ACKNOWLEDGMENTS

We acknowledge fruitful discussions with D. Ertas and L. Goren. This project has received funding from the European Union's Seventh Framework Programme for research, technological development and demonstration under Grant Agreement No. 316889.

APPENDIX: ORTHOGONALITY RELATIONS

Here we show that the functions

$$q_n(y) = J_{2/3}\left(\kappa_n\left(\frac{y}{h}\right)^{3/4}\right), \quad n = 1,\ldots,\infty \tag{A1}$$

form an orthogonal system relative to the scalar product $(a,b) = \int_0^h ab\sqrt{y}dy$. This in turn allows us to derive Eq. (14). The functions q_n are solutions of Eq. (8),

$$\frac{d^2(\sqrt{y}q_n)}{dy^2} = -\frac{9\kappa_n^2}{16h^{3/2}}q_n, \tag{A2}$$

which satisfy the following boundary conditions, corresponding to the boundary conditions 7(a) and 7(b):

$$\lim_{y\to 0}\sqrt{y}q_n(y) = 0, \quad \frac{d(\sqrt{y}q_n)}{dy}(h) = 0. \tag{A3}$$

In the following we evaluate the integral $\int_0^h \frac{d^2(\sqrt{y}q_i)}{dy^2}q_j\sqrt{y}dy$ in two ways. First, we use Eq. (A2),

$$\int_0^h \frac{d^2(\sqrt{y}q_i)}{dy^2}q_j\sqrt{y}dy = -\frac{9\kappa_i^2}{16h^{3/2}}\int_0^h q_iq_j\sqrt{y}dy. \tag{A4}$$

Second, we apply a double integration by parts

$$\begin{aligned}\int_0^h \frac{d^2(\sqrt{y}q_i)}{dy^2}q_j\sqrt{y}dy &= \int_0^h \sqrt{y}q_i\frac{d^2(\sqrt{y}q_j)}{dy^2}dy \\ &= -\frac{9\kappa_j^2}{16h^{3/2}}\int_0^h q_iq_j\sqrt{y}dy,\end{aligned} \tag{A5}$$

where the surface terms vanish because of the boundary conditions (A3). Since $\kappa_i \neq \kappa_j$ for $i \neq j$, a comparison of Eqs. (A4) and (A5) implies orthogonality of the functions q_n,

$$\int_0^h q_iq_j\sqrt{y}dy = \delta_{ij}\int_0^h q_j^2\sqrt{y}dy, \tag{A6}$$

where δ_{ij} is the Kronecker delta.

Initial condition for shear rate

The solution for shear rate $\dot{\gamma}$ [Eq. (9)] is a linear combination of q_n functions with weights b_n that need to be determined from the initial condition

$$\dot{\gamma}(y,t=0) = -\frac{dv^0}{dy}, \tag{A7}$$

corresponding to Eq. 7(c). Multiplying Eq. (9) for $t = 0$ by $b_i\sqrt{y}$ and integrating over the range of $y \in (0,h)$ leads, after some rearrangement, to

$$b_i = \begin{cases} -\frac{\int_0^h(\sqrt{y}dv^0/dy + b^*y)q_idy}{\sqrt{h}\int_0^h q_i^2\sqrt{y}dy}, & \theta > \theta_r \quad \text{(A8a)} \\ -\frac{\int_0^h \sqrt{y}dv^0/dyq_idy}{\sqrt{h}\int_0^h q_i^2\sqrt{y}dy}, & \theta < \theta_r, \quad \text{(A8b)} \end{cases}$$

where the sum was reduced to a single term due to Eq. (A6). The last equation is identical to Eq. (14).

[1] Y. Forterre and O. Pouliquen, Annu. Rev. Fluid Mech. **40**, 1 (2008).
[2] E. Aharonov and D. Sparks, Phys. Rev. E **60**, 6890 (1999).
[3] E. Aharonov and D. Sparks, Phys. Rev. E **65**, 051302 (2002).
[4] L. E. Silbert, D. Ertas, G. S. Grest, T. C. Halsey, D. Levine, and S. J. Plimpton, Phys. Rev. E **64**, 051302 (2001).
[5] O. Pouliquen, Phys. Fluids **11**, 542 (1999).
[6] C. Ancey, Phys. Rev. E **65**, 011304 (2001).
[7] R. A. Bagnold, Proc. R. Soc. London Ser. A **225**, 49 (1954).
[8] G. D. R. MiDi, Eur. Phys. J. E **14**, 341 (2004).
[9] F. da Cruz, S. Emam, M. Prochnow, J.-N. Roux, and F. Chevoir, Phys. Rev. E **72**, 021309 (2005).
[10] P. Jop, Y. Forterre, and O. Pouliquen, Nature (London) **441**, 727 (2006).
[11] A. J. Holyoake and J. N. McElwaine, J. Fluid Mech. **710**, 35 (2012).
[12] N. Mitarai and H. Nakanishi, Phys. Rev. Lett. **94**, 128001 (2005).
[13] Z.-T. Wang, Granular Matter **6**, 67 (2004).
[14] D. Ertas, G. S. Grest, T. C. Halsey, D. Levine, and L. E. Silbert, Europhys. Lett. **56**, 214 (2001).
[15] Z. Shojaaee, J.-N. Roux, F. Chevoir, and D. E. Wolf, Phys. Rev. E **86**, 011301 (2012).
[16] E. Aharonov and D. Sparks, J. Geophys. Res. **109**, B09306 (2004).
[17] J. R. Rice, J. Geophys. Res. **111**, B05311 (2006).
[18] Z. Shojaaee, L. Brendel, J. Torok, and D. E. Wolf, Phys. Rev. E **86**, 011302 (2012).
[19] S. B. Savage and K. Hutter, J. Fluid Mech. **199**, 177 (1989).
[20] R. M. Iverson and R. P. Denlinger, J. Geophys. Res. **106**, 537 (2001).
[21] R. P. Denlinger and R. M. Iverson, J. Geophys. Res. **106**, 553 (2001).
[22] O. Pouliquen and Y. Forterre, J. Fluid Mech. **453**, 133 (2002).
[23] A. Mangeney, P. Heinrich, and R. Roche, Pure Appl. Geophys. **157**, 1081 (2000).
[24] G. Faccanoni and A. Mangeney, Int. J. Num. Anal. Meth. Goemech. **37**, 1408 (2013).
[25] H. Capart, C.-Y. Hung, and C. P. Stark, J. Fluid Mech. **765**, R4 (2015).
[26] L. E. Silbert, J. W. Landry, and G. S. Grest, Phys. Fluids **15**, 1 (2003).
[27] C. S. Campbell and C. E. Brennen, J. Fluid Mech. **151**, 167 (1985).
[28] C. Y. Lo, M. D. Bolton, and Y. P. Cheng, Granular Matter **12**, 477 (2010).
[29] O. Katz, J. Morgan, E. Aharonov, and B. Dugan, Geomorphology **220**, 104 (2014).
[30] A. Taboada and N. Estrada, J. Geophys. Res. **114**, F03004 (2009).
[31] Z. Liu and H. Koyi, Landslides **10**, 139 (2013).
[32] J. Morgan and P. McGovern, J. Geophys. Res. **110**, B05402 (2005).
[33] C. Campbell, P. Cleary, and M. Hopkins, J. Geophys. Res. **100**, 8267 (1995).
[34] M. Boas, *Mathematical Methods in the Physical Sciences* (Wiley, New York, 2006).
[35] M. Abramowitz and I. A. Stegun, *Handbook of Mathematical Functions with Formulas, Graphs, and Mathematical Tables* (Dover, New York, 1972).
[36] P. A. Cundall and O. D. Strack, Geotechnique **29**, 47 (1979).
[37] J. Schafer, S. Dippel, and D. E. Wolf, J. Phys. (France) I **6**, 5 (1996).
[38] L. Goren, E. Aharonov, D. Sparks, and R. Toussaint, Pure Appl. Geophys. **168**, 2289 (2011).
[39] J. K. Morgan, J. Geophys. Res. **104**, 2721 (1999).
[40] N. Makedonska, D. W. Sparks, E. Aharonov, and L. Goren, J. Geophys. Res. **116**, B09302 (2011).
[41] D. Frenkel and B. Smit, *Understanding Molecular Simulations* (Academic Press, San Diego, 2002).
[42] K. Kamrin and D. L. Henann, Soft Matter **11**, 179 (2015).
[43] K. Kamrin and G. Koval, Phys. Rev. Lett. **108**, 178301 (2012).